CrossMark

RESEARCH ARTICLE

Exploring Vertical Turbulence Structure in Neutrally and Stably Stratified Flows Using the Weather Research and Forecasting–Large-Eddy Simulation (WRF–LES) Model

Mireia Udina[1] · **Jielun Sun[2]** · **Branko Kosović[2]** ·
Maria Rosa Soler[1]

Abstract Following Sun et al. (J Atmos Sci 69(1):338–351, 2012), vertical variations of turbulent mixing in stably stratified and neutral environments as functions of wind speed are investigated using the large-eddy simulation capability in the Weather Research and Forecasting model. The simulations with a surface cooling rate for the stable boundary layer (SBL) and a range of geostrophic winds for both stable and neutral boundary layers are compared with observations from the Cooperative Atmosphere–Surface Exchange Study 1999 (CASES-99). To avoid the uncertainty of the subgrid scheme, the investigation focuses on the vertical domain when the ratio between the subgrid and the resolved turbulence is small. The results qualitatively capture the observed dependence of turbulence intensity on wind speed under neutral conditions; however, its vertical variation is affected by the damping layer used in absorbing undesirable numerical waves at the top of the domain as a result of relatively large neutral turbulent eddies. The simulated SBL fails to capture the observed temperature variance with wind speed and the observed transition from the SBL to the near-neutral atmosphere with increasing wind speed, although the vertical temperature profile of the simulated SBL resembles the observed profile. The study suggests that molecular thermal conduction responsible for the thermal coupling between the surface and atmosphere cannot be parameterized through the Monin–Obukhov bulk relation for turbulent heat transfer by applying the surface radiation temperature, as is common practice when modelling air–surface interactions.

Keywords Boundary-layer turbulence · Large-eddy simulation · Stable boundary layer · Weather Research and Forecasting model

✉ Mireia Udina
  mudina@am.ub.es

[1] Dept. Astronomia i Meteorologia, Universitat de Barcelona, C/Martí i Franquès, 1., 08028 Barcelona, Spain

[2] National Center for Atmospheric Research, Boulder, CO, USA

⚛ Springer

1 Introduction

The atmospheric stable boundary layer (SBL) is commonly formed when the ground is cooled by longwave radiation at night with low wind speeds (Stull 1988). Understanding of the SBL has been improved through field campaigns, for example, the Stable Atmospheric Boundary-Layer Experiment in Spain 1998 (SABLES98) (Cuxart et al. 2000), the Cooperative Atmosphere–Surface Exchange Study 1999 (CASES-99) (Poulos et al. 2002), and the Stable Atmospheric Boundary-Layer Experiment in Spain 2006 (SABLES2006) (Yagüe et al. 2007). However, mesoscale models still perform poorly in simulating the SBL, and large-eddy simulation (LES) still cannot simulate realistically the strongly stable atmosphere.

Mahrt (1998) classified the SBL into weakly stable, transitional stable, and very stable regimes based on the variation of the sensible heat flux with stability. Recently, Sun et al. (2012) (S12 hereinafter) investigated the month-long nocturnal CASES-99 dataset from a 60-m tower, and found two main turbulence regimes for given height above ground (z) in terms of the relationship between turbulent intensity expressed in terms of variances of wind components and horizontal wind speed, $V(z)$. Regime 1 in S12 is characterized by weak turbulence generated by shear over a finite $\delta z < z$, i.e., $\delta V/\delta z$, in the stably stratified atmosphere when $V(z)$ is less than its threshold value, $V_s(z)$. Regime 2 in S12 is characterized by strong turbulence generated by bulk shear $V(z)/z$, i.e., $\delta z = z$, when $V(z) > V_s(z)$. As the strong turbulence regime is dominated by large coherent eddies that scale with z, the layer below z is well mixed and the vertical temperature gradient is small; i.e., the strong turbulence regime is the near-neutral regime. Sun et al. (2015, 2016) (the latter, S16 hereinafter) found that the dramatic transition of turbulence intensity between the stable and near-neutral regimes at night can be explained by the hockey-stick transition (HOST) hypothesis, so named as the transition resembles a hockey stick. By applying the concept of the coupling between turbulent kinetic energy (TKE) and turbulent potential energy (TPE), which is related to temperature fluctuations, based on Ostrovsky and Troitskaya (1987) and Zilitinkevich et al. (2007), S16 explained that, in the stably stratified atmosphere, a significant portion of the shear-generated turbulent energy is used to increase TPE through turbulent heat transfer, thus TKE increases weakly with $V(z)$. In the nearly neutral atmosphere, temperature fluctuations in the form of TPE are reduced significantly as a result of the reduced heat transfer from the reduced stable stratification. As a result, the shear-generated turbulent energy leads directly to the enhanced increase of TKE with $V(z)$ in the nearly neutral regime. In other words, the threshold wind $V_s(z)$ represents an averaged critical shear needed to reduce the vertical temperature gradient significantly below z. Therefore, temperature fluctuations increase with $V(z)$ in association with the increase of TPE in the stable regime, and decrease with $V(z)$ due to the decrease of TPE in the near-neutral regime. Besides the two main turbulent regimes at given a z, occasionally relatively strong turbulent intensity for $V(z) < V_s(z)$ may occur when turbulence is generated by large disturbing events above the surface, such as breaking waves beneath a low-level jet (LLJ) (Fig. 2 in S12).

The current study investigates the relationship between turbulent intensity and wind speed by using the LES mode of the Weather Research and Forecasting (WRF–ARW) model (Skamarock et al. 2008), i.e., WRF–LES (Moeng et al. 2007; Mirocha et al. 2010), especially beyond the lower 60-m layer observed during CASES-99. Large-eddy simulation modelling has been used to study SBL characteristics (Mason and Derbyshire 1990; Brown et al. 1994; Andren 1995; Kosović and Curry 2000; Saiki et al. 2000; Jimenez and Cuxart 2005; Basu and Port-Agel 2006; Beare et al. 2006; Huang and Bou-Zeid 2013), and all of the simulated SBL cases produced a continuous turbulent boundary layer in moderately stable conditions;

For example, Beare et al. (2006) (B06 hereinafter) conducted an LES model intercomparison study for the SBL as part of the Global Energy and Water Cycle Experiment Atmospheric Boundary Layer Study (GABLS) project. All the LES models in B06 were driven by a fixed cooling rate with initial conditions consistent with the Beaufort Sea Arctic Stratus Experiment (BASE) observation.

Previous WRF–LES model studies have improved the subgrid-scale (SGS) model performance (Mirocha et al. 2010; Kirkil et al. 2012) including the non-linear backscatter and anisotropy model (Kosović 1997). Other studies used LES nested in the WRF model domain by either two- (Moeng et al. 2007) or one-way nesting (Liu et al. 2011; Mirocha et al. 2013; Talbot et al. 2012; Muñoz-Esparza et al. 2014) in the unstable atmosphere only. One of the advantages of using the WRF–LES model is its ability to simulate the atmosphere over realistic terrain (Talbot et al. 2012). Similar to other LES models in the literature, the WRF–LES model is designed to directly resolve large eddies that dominate turbulent energy and parametrize the effect of small eddies with the SGS models. The WRF–LES model provides a useful tool to investigate the non-linear dynamics of turbulence. Because turbulent eddies are much smaller in the SBL than in the convective boundary layer (CBL), simulating the SBL requires a high-resolution grid with an accurate SGS model as well as high computational resources.

In Sect. 2, we describe the WRF–LES model and the methodology. We validate the WRF–LES model against the GABLS case described by B06 in Sect. 3, as the WRF–LES model has not yet been evaluated for the SBL. We describe general characteristics of simulated neutral and stable boundary layers in Sect. 4, and examine the dependence of turbulent intensity and turbulent temperature fluctuations on wind speed and their vertical variations associated with the structure of turbulent eddies in Sect. 5. We discuss physical processes in the simulation that lead to differences between the simulated and observed neutral and stable boundary layers in Sect. 6. Finally, we summarize with conclusions in Sect. 7.

2 Methodology

The large-eddy simulations are carried out using the WRF–LES model version 3.4 (Moeng et al. 2007; Mirocha and Kosović 2010; Mirocha et al. 2013). A numerical filter is applied to obtain resolved variables associated with large energetic eddies. The effect of small-scale turbulence, i.e., the SGS turbulence, on resolved variables is parametrized with a linear eddy viscosity approach using a prognostic equation for TKE based on the Smagorinsky model (Smagorinsky 1963; Lilly 1967), which is a 1.5-order TKE model (Mirocha et al. 2014). Because the subgrid contribution to turbulence is important near the surface or when the atmosphere is strongly stable, and assumptions in parametrizing the subgrid turbulence vary with different subgrid schemes, the NBA subgrid scheme, which includes non-linear terms for the anisotropy and the energy backscatter of the subgrid stress tensor, is also used to investigate the subgrid contribution to turbulent variables near the surface. The fifth-order finite-differencing advection scheme is chosen for horizontal advection, the third order for vertical advection, and the third-order Runge–Kutta scheme for time integration. A Coriolis parameter of $f = 0.0001\,\text{s}^{-1}$ ($\approx 45°\text{N}$) is used.

The domain size is $1\,\text{km} \times 1\,\text{km}$ in the horizontal directions (x, y) and $600\,\text{m}$ in the vertical (z), with 200 grid points in both x and y directions and 100 levels in z with a flat surface. The horizontal grid spacing ($\Delta x = \Delta y$) is $5\,\text{m}$, and the vertical resolution (Δz) is $1.8\,\text{m}$ in the bottom 20 levels and is stretched with z above such that $\Delta z = 3.3\,\text{m}$ at level 40 and $\Delta z = 10\,\text{m}$

at level 80. The lateral boundary conditions are periodic. The simulated flow is in response to a constant horizontal pressure gradient throughout the domain. The Monin-Obukhov bulk relation is used to estimate the momentum and heat fluxes at the surface, i.e.,

$$\overline{w'V'} = C_d V^2, \qquad (1)$$

$$\overline{w'\theta'} = C_h V(\theta_s - \theta_a), \qquad (2)$$

where $V = \sqrt{u^2 + v^2}$ is the horizontal wind speed, u, v, and w are the wind components in x, y, and z directions, θ is the potential air temperature, θ_s is the surface radiation temperature, θ_a is θ at the first grid level of 1.8 m, the prime represents the perturbation from the temporal mean expressed by the overline, and C_d and C_h are the exchange coefficients for momentum and heat, respectively, which are functions of stability and their corresponding surface roughnesses (e.g., Garratt 1992). A damping layer is added in a top layer of the domain to absorb undesirable numerical waves, while the initial wind speed is set equal to a selected geostrophic wind speed. Two tasks—(i) reproducing the GABLS SBL in B06, and (ii) simulating the neutral and stable atmosphere—are labelled as WRF–LES–GABLS and WRF–LES–EVTS (WRF–LES–exploring vertical turbulence structure). Initial conditions for the two tasks are described below:

 (i) The initial conditions for simulating the WRF–LES–GABLS case are taken from B06. The initial potential temperature is set to 265 K from the surface up to 100 m and to increase at 0.01 K m^{-1} to 270 K at $z = 600$ m. The initial specific humidity (q) is set to 2 g kg^{-1} for the lower 375 m and to 1 g kg^{-1} above. The geostrophic wind components in the x and y directions are $U_g = 8$ m s^{-1} and $V_g = 0$; the surface cooling rate is 0.25 K h^{-1}; a damping layer of 300 m is added from $z = 300$ m to $z = 600$ m.

(ii) For the WRF–LES–EVTS simulations, the initial θ is set to 290 K from the surface up to 175 m, to increase at 0.01 K m^{-1} between 175 and 375 m, and to be 292 K above 375 m. The initial q is set to 10 g kg^{-1} for the lower 175 m, to decrease linearly to 4 g kg^{-1} from 175 to 225 m, and remains at 4 g kg^{-1} above 225 m. The aerodynamic roughness length z_0 is set to 0.05 m, which is derived from the CASES-99 observation (Sun 2011), and 0.5 m for a sensitivity test. The surface is set with two surface cooling rates (Table 1): zero cooling at the surface corresponding to neutral condition, and the same cooling rate of 0.25 K h^{-1} as in B06 corresponding to a steadily cooled surface for simulating the SBL. Four values of geostrophic wind speed, $V_g = 16.5, 13.75, 11$, and 8.25 m s^{-1}, referred to as A, B, C, and D, are used to represent the horizontal pressure gradient imposed throughout the vertical domain to drive turbulent mixing in the atmospheric boundary layer (ABL) (Table 1). Thus, a total of eight WRF–LES–EVTS simulations are obtained: four for the neutral condition (A-neutral, B-neutral, C-neutral, and D-neutral), and four for the SBL (A-stable, B-stable, C-stable, and D-stable). The minimum value of V_g is chosen such that turbulence near the surface is resolved with the prescribed cooling rate without the runaway cooling problem described by, for example, Derbyshire (1990) and Jimenez and Cuxart (2005). A 200-m damping layer is added between $z = 400$ m and $z = 600$ m. Because of geostrophic forcing, the equilibrium flow is primarily along the y-axis for all the WRF–LES–EVTS cases, i.e., $V \approx v$ and $u \approx 0$ (Sect. 4).

All simulations are run for 9 h to allow the development of the boundary layer to reach a quasi-steady state, and calculated fields every 10 s from the last simulation hour are used for analyses. A mean resolved variable at each height z is calculated as the average value over the 200×200 grid points for the last simulation hour. A second-moment resolved variable at each z is calculated as the 5-min average of covariances at the 200×200 grid points, where the covariance at each grid point is calculated as the product of perturbations of two variables

from their means over the 200×200 grid points. Increasing the averaging temporal intervals to 10 min does not change the result significantly, suggesting that most of the turbulence eddies are captured within 5-min segments, and turbulence at the ninth hour is relatively stationary. A total variable of the second-order moment is then calculated as the sum of the resolved and the subgrid parametrized components. Variables of the second moment used herein are all total variables unless otherwise stated. The w skewness at height z is given by $\overline{w'^3}(z) = \sum_{i=1}^{N}[w_i(z) - \bar{w}(z)]^3/[(N-2)\sigma_w^3(z)]$, where $N = 200 \times 200 \times 6 \times 5 \times 12$ is the number of data points over 5 min and $\sigma_w(z)$ is the standard deviation of w. The momentum flux is calculated as $|\overline{w'V'}(z)| = [\overline{w'u'}^2(z) + \overline{w'v'}^2(z)]^{1/2}$. In addition to the heat flux $\overline{w'\theta'}$, we also investigate the temperature scale $\theta_*(z) \equiv -\overline{w'\theta'}(z)/u_*(z)$, where $u_*(z) = |\overline{w'V'}(z)|^{1/2}$. Turbulent kinetic energy at each height z is calculated as $\mathrm{TKE}(z) = (1/2)[\sigma_u^2(z) + \sigma_v^2(z) + \sigma_w^2(z)]$, where $\sigma_u^2(z)$, $\sigma_v^2(z)$, and $\sigma_w^2(z)$ are the variances of the three wind components. The SBL height, h, is estimated as the height at which the momentum flux decreases to 5 % of its surface value divided by 0.95, following Kosović and Curry (2000).

3 WRF–LES Model Validation in the SBL

Here, we compare simulated results between the WRF–LES model and the LES models used in B06 for their Arctic stable boundary layer case. The spatial resolution of $\Delta x = \Delta y = 6.25$ m in the B06 models is comparable to the $\Delta x = \Delta y = 5$ m used in the WRF–LES model.

In general, the WRF–LES simulated wind and temperature profiles compare well with those from B06 (Fig. 1). Both momentum and heat fluxes from the WRF–LES model are at the lower end of the simulated results in B06 (Fig. 2a, b). As a result, the height of the super-geostrophic jet and the SBL height, $h = 147$ m, from the WRF–LES model are at
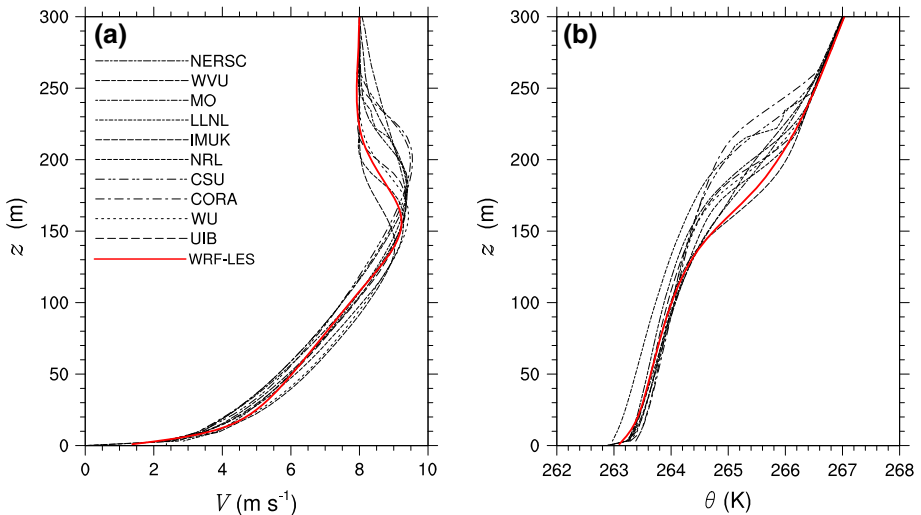
Fig. 1 Vertical profiles of spatial- and temporal-averaged **a** horizontal wind speed (V) and **b** potential temperature (θ) from the WRF–LES model (*red line*) compared with those from the GABLS intercomparison in B06, where the LES model acronyms are described
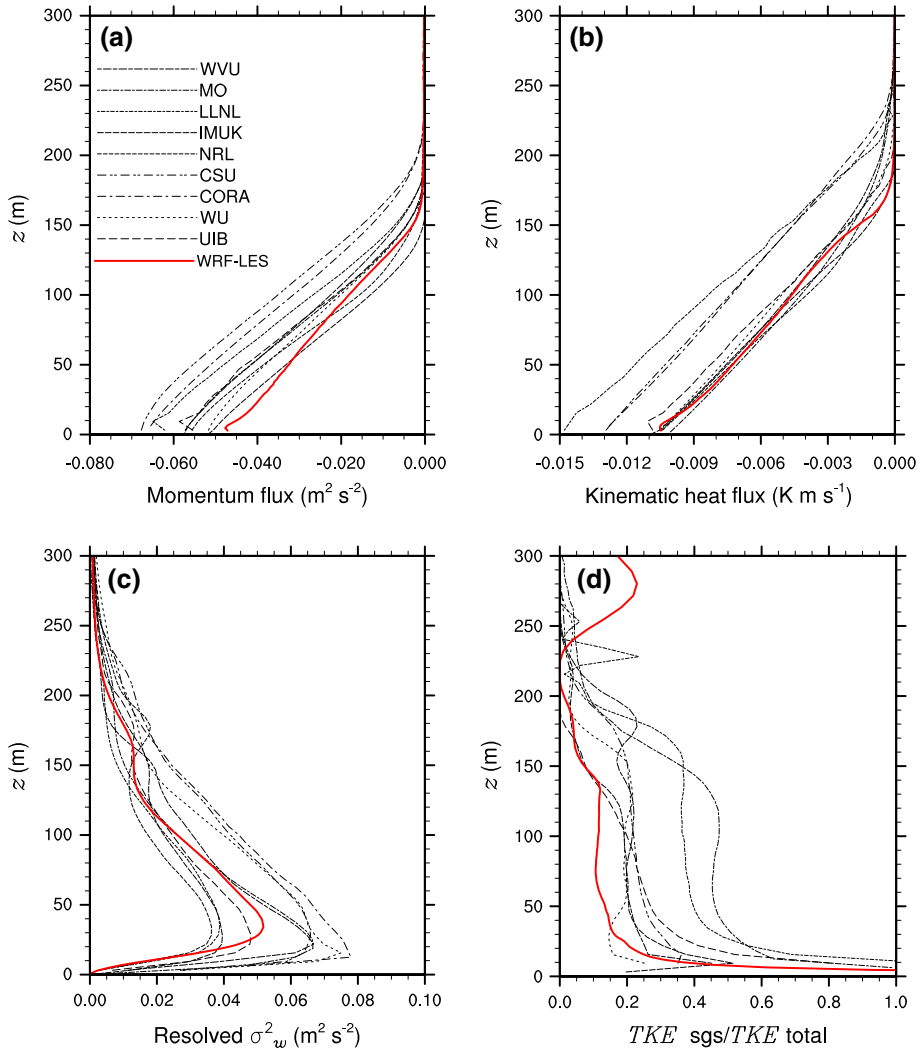
Fig. 2 The same as Fig. 1 except for **a** the total momentum flux, **b** the total heat flux, **c** the resolved vertical velocity variance (σ_w^2), and **d** the ratio between the subgrid (sgs) and total TKE

the lower end of the simulated values from B06. The vertical velocity variance σ_w^2 (Fig. 2c) from the WRF–LES model is well resolved, with its maximum at tens of metres above the surface and its approach to zero at $z = 0$, which is also similar to the results from the other models in B06. In addition, as observed by S16, TKE is dominated by small eddies near the surface, and the subgrid contribution of TKE to the total TKE decreases with height, which is similar to the other models in B06 (Fig. 2d). Compared with the other LES models, the ratio of the subgrid to the total TKE from the WRF–LES model decreases fastest, reaching around 10–15 % above ≈ 40 m. The above comparisons suggest that the performance of the WRF–LES model is comparable to that of the other LES models in B06 for simulating the SBL.

Table 1 Boundary-layer characteristics of the WRF–LES–EVTS simulations

| Simulation	Cooling rate ($K h^{-1}$)	V_g ($m s^{-1}$)	h (m)	u_{*s} ($m s^{-1}$)	H_s ($W m^{-2}$)
A-neutral	0	16.5	466.1	0.588	0
B-neutral	0	13.75	439.6	0.510	0
C-neutral	0	11	427.0	0.409	0
D-neutral	0	8.25	402.5	0.314	0
A-stable	0.25	16.5	402.1	0.501	−35.08
B-stable	0.25	13.75	336.3	0.404	−28.44
C-stable	0.25	11	240.4	0.316	−21.27
D-stable	0.25	8.25	169.3	0.220	−13.35

4 Vertical Variations of Simulated Turbulence in Neutral and Stable Boundary Layers

The main characteristics of the SBL in the WRF–LES–EVTS simulations with the forcing associated with four geostrophic wind speeds (A, B, C, and D), and the surface cooling of zero (neutral) and a constant value (stable), are summarized in Table 1, where the surface friction velocity u_{*s} and the surface heat flux $H_s = \rho C_p (\overline{w'\theta'})_s$ (where the subscript "s" indicates the value at the surface) are included. The values of u_{*s} and H_s for the most stable case (D-stable) are similar to those from LES SBL simulations found in literature (e.g., Beare et al. 2006; Huang and Bou-Zeid 2013), which correspond to the continuously turbulent SBL under moderately stable conditions observed in CASES-99 (e.g., Van de Wiel et al. 2003).

Because of the surface drag acting as the momentum sink, the downward momentum fluxes decrease from the surface up to the top of the ABL (Fig. 4a), and wind speed increases with height, z, for all four V_g values (Fig. 3a). As the horizontal pressure gradient increases with V_g, the enhanced turbulent mixing leads to increasing h with V_g under both neutral and stable conditions (Table 1; Fig. 3a). We next discuss the simulated wind and temperature profiles with two different surface coolings separately. To contrast the development of the neutral and the stable boundary layers, we compare differences in wind profiles between the neutral and stable simulations. We then describe vertical variations of turbulent variables for both neutral and stable simulations.

4.1 Wind and Temperature Profiles in Neutral Simulations

As no heat is added to or removed from the surface with zero surface cooling, the temperature in the domain reaches an approximately constant value below the damping layer, which is the approximate vertically integrated mean value of the initial temperature profile (dotted black line in Fig. 3b). The relatively well-mixed temperature profile indicates that shear-generated turbulent eddies forced by the horizontal pressure gradient through V_g are relatively large, and are capable of transporting heat across the initial temperature inversion layer between 175 m and 375 m after 9 h into each simulation. As a result, the temperature is higher than its initial value in the lower half of the domain and lower in the top half. At this quasi-steady state, the sensible heat flux is reduced to a small, but nonzero, value as the vertical temperature gradient is small (Fig. 4b) (see below for more details). In the damping layer, the temperature increases with height slightly. As a result of the vertical variation of the vertical temperature
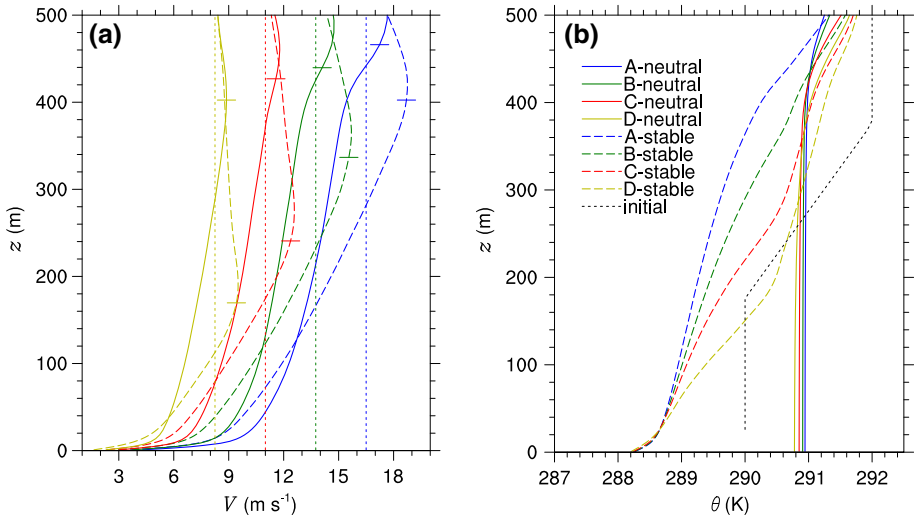
Fig. 3 Vertical profiles of **a** horizontal wind speed (V) and **b** potential temperature (θ) in response to the four geostrophic wind speeds (A, B, C, and D) with zero (*solid lines*) and the constant (*dashed lines*) surface cooling rates. In **a**, the four *vertical dashed lines* correspond to the initial geostrophic wind speed V_g, and the *horizontal lines* indicate the calculated top of the boundary layer for each simulation (h). In **b**, the initial θ is marked with *black dashed line*
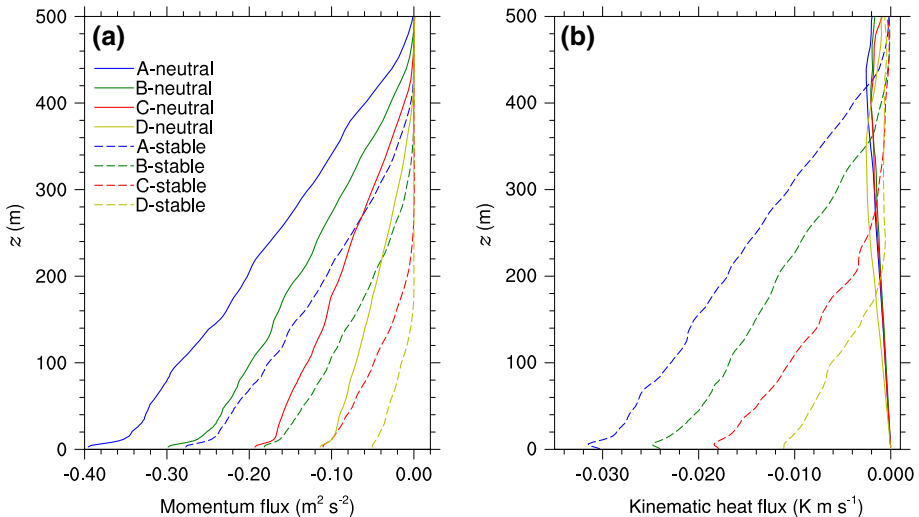
Fig. 4 Vertical profiles of **a** momentum fluxes and **b** heat fluxes in response to the four geostrophic wind speeds (A, B, C, and D) with zero (*solid lines*) and the constant (*dashed lines*) surface cooling rates

gradient, the wind speed reaches its maximum at the bottom of the damping layer for the strongest V_g due to the vertical convergence of the momentum flux from the sharp decrease of the momentum transfer (Fig. 4a). As shear decreases with decreasing V_g, as does the turbulence intensity and the size of turbulence eddies (S16), the temperature field is less well mixed with decreasing V_g below the damping layer, and the height of the super-geostrophic jet decreases with decreasing V_g.

## 4.2 Wind and Temperature Profiles in Stable Simulations

In general, the vertical structure of the wind speed and potential temperature under stable conditions (Fig. 3) agrees well with the SBL equilibrium model developed by Nieuwstadt (1985). The equilibrium wind speed $V(z)$ for each simulation increases with z and reaches its maximum near the SBL top, h (Fig. 3a). When the surface temperature, θ_s, in Eq. 2 is lowered at the constant cooling rate of $0.25\,\mathrm{K\,m^{-1}}$, heat above the surface is steadily removed through the downward sensible heat flux, and the initial θ is reduced. As a result of the surface heat sink, the downward heat transfer decreases with height (Fig. 4b), and the SBL develops near the surface (Fig. 3b). Because wind speed at a given z increases with V_g (Fig. 3a) and the sensible heat flux is linearly proportional to wind speed in Eq. 2, the simulated surface sensible heat flux increases with increasing V_g at a given z (Fig. 4b). As $V(z)$ is small near the surface, so is the sensible heat flux; based on heat conservation, the air temperature near the surface is strongly controlled by the surface temperature θ_s, and does not vary much with V_g (Fig. 3b). As the downward sensible heat flux increases with increasing V_g, the cold air is transported higher with the stronger downward heat flux, leading to the increase of the SBL depth, h, with increasing V_g, as shown in Fig. 3a and Table 1.

4.3 Comparison of Wind Profiles Between Simulated Stable and Neutral Boundary Layers

Comparison of $V(z)$ between the neutral and stable cases for given V_g indicates that the rate of the $V(z)$ increase with z is larger under the neutral conditions than under stable conditions in the lower ABL; the situation is reversed in the upper ABL (Fig. 3a). This vertical variation of $V(z)$ between the neutral and stable cases can be explained by the turbulent energy variation in TKE and TPE described in Sect. 1. Because of the heat transfer associated with the surface cooling, part of the shear-generated turbulent energy is used in increasing TPE, i.e., mainly temperature variances, through the heat transfer at the expense of lesser increase in TKE, i.e., less increase of the downward momentum flux with height (Fig. 4a), leading to the weak increase of $V(z)$ with height. While for the neutral cases, the initial vertical temperature gradient approaches a small value and the temperature within the domain approaches a nearly constant value, shear-generated turbulent mixing then leads to the direct increase of any TKE-related variable, including momentum fluxes, without being consumed to TPE. As a result, for given V_g, the magnitude of the momentum flux and $V(z)$ at a given z are smaller for the stable case than for the neutral case in the lower ABL (Figs. 3a, 4a). However, because the size of turbulent eddies decreases with increasing stable stratification as demonstrated in S16 (see Sect. 5.2 for more details), relatively large coherent eddies transport the relatively low-momentum air near the surface to a higher altitude in the neutral environment than in the stable environment. As a result, wind speed for given V_g is larger in the stable case than in the neutral case in the upper ABL, in contrast to the vertical variation of horizontal wind speed in the lower ABL.

4.4 Vertical Variations of Wind-Speed Variances and w Skewness

Because the forcing of the flow, V_g, is along the y-axis, and the wind-direction rotation with z as a result of the Coriolis force is negligibly small in all the WRF–LES–EVTS simulations, we only compare the wind-speed variance in y-direction, σ_v^2, between the stable and neutral cases (Fig. 5a). Consistent with the momentum and heat-flux profiles, σ_v^2, σ_w^2, and TKE decrease gradually with z for all the WRF–LES–EVTS cases until they are nearly zero at
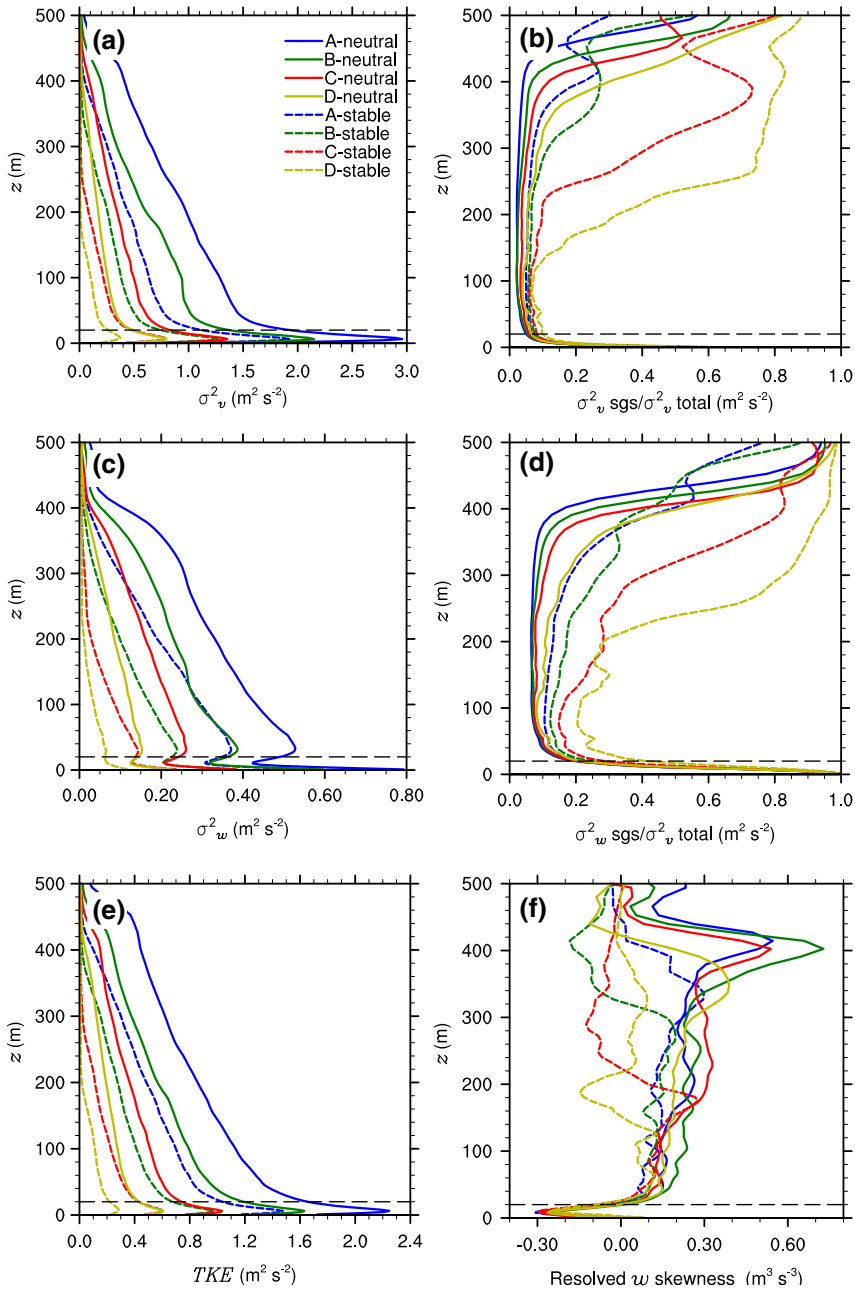
Fig. 5 Vertical profiles of **a** the wind-speed variance in y direction, $\sigma_v^2(z)$, **b** the ratio between the subgrid and total $\sigma_v^2(z)$, **c** the vertical wind-speed variance, $\sigma_w^2(z)$, **d** the ratio between the subgrid and total $\sigma_w^2(z)$, **e** turbulent kinetic energy, $TKE(z)$, and **f** the vertical wind component skewness $\overline{w'^3}(z)$ in response to the four geostrophic wind speeds (A, B, C, and D) with zero (*dashed lines*) and the constant (*solid lines*) surface cooling rates. The *black horizontal dashed line* in each panel indicates the limiting height where $\overline{w'^3}(z)$ becomes positive, and the contribution of the subgrid variances to their total variances decreases significantly

the top of the ABL, partly due to the damping layer at the top (Figs. 5a, c, e). As in previous LES studies (e.g., Andren 1995; Kosović and Curry 2000), σ_v^2 for all the WRF–LES–EVTS cases reaches its maximum about 10 m above the surface, which is below the maximum of σ_w^2, and the magnitude of σ_v^2 is larger than for σ_w^2 for each case.

For each simulation, the contributions of both subgrid σ_v^2 and σ_w^2 to their total components are largest at the surface and decrease with z up to about the bottom of the damping layer at $z = 400$ m for the neutral cases and below $z = 400$ m for the stable cases (Figs. 5b, d). The subgrid σ_w^2 and σ_v^2 contribute almost 100 % and about 40 %, respectively, to their totals at the surface, which suggests that the subgrid contributions dominate the resolved turbulence components near the surface, as the WRF model completely resolves only eddies greater than $6\Delta x - 7\Delta x$ (Skamarock 2004). Although the small size of turbulence eddies near the surface has been observed in S16, the unrealistic negative resolved w skewness below $z = 20$ m in Fig. 5f implies that the subgrid parametrization may have issues, which cannot be resolved even with the NBA subgrid scheme (Mirocha et al. 2010). Therefore, we limit investigation to the vertical domain above $z = 20$ m.
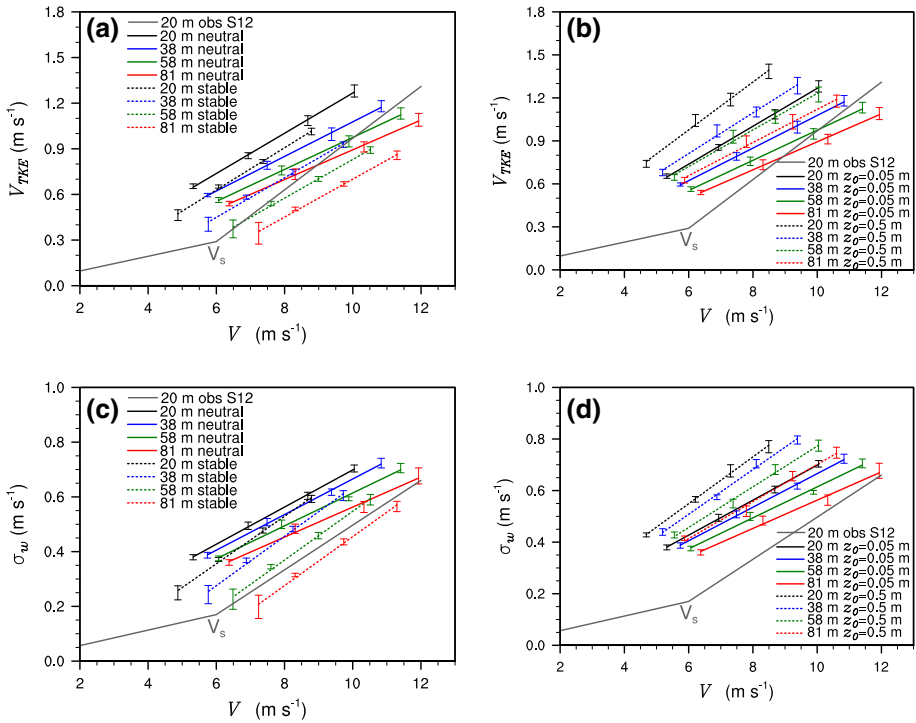
5 Vertical Variation of Relationships Between Turbulent and Mean Variables

Here, we explore the vertical variation of the relationship between turbulent intensity and horizontal wind speed from the WRF–LES–EVTS simulations in comparison with those in S12. As in S12, turbulent intensity is expressed as the square root of TKE, $V_{\text{TKE}}(z) = \sqrt{TKE(z)}$, and the standard deviation of the vertical velocity, σ_w.

5.1 Turbulence Intensity as a Function of Wind Speed

By applying the four values of V_{g}, turbulence intensity including $V_{\text{TKE}}(z)$ and $\sigma_w(z)$ is investigated as a function of wind speed $V(z)$ for the neutral and stable conditions. The relationships between $V_{\text{TKE}}(z)$ and $V(z)$ and between $\sigma_w(z)$ and $V(z)$ at $z \approx 20, 40, 60,$ and 80 m are all approximately linear and are linearly regressed from the WRF–LES–EVTS simulations for the four values of V_{g} (Fig. 6a, c). The simulated relationships for both stable and neutral conditions shift toward higher wind speed as height increases, which is similar to the results for the near-neutral regime in S12. By examining the increasing rates of $V_{\text{TKE}}(z)$ and $\sigma_w(z)$ with $V(z)$, i.e., the slopes of the $V_{\text{TKE}}(z)-V(z)$ and $\sigma_w(z)-V(z)$ relationships, at z from 20 m up to 120 m, we find that they decrease steadily with z, while the observed rates in S12 remain relatively constant with z and only decrease slightly with z towards the highest observation height of 60 m (Fig. 7). Different from the observation in S12, the slope of the relationship between the turbulent intensity and wind speed is larger for the stable than for the neutral case. Increasing the surface roughness length from $z_0 = 0.05$ m to $z_0 = 0.5$ m, for example, in the neutral case to estimate the exchange coefficient for the surface momentum in Eq. 1 does enhance the rate of increase for both V_{TKE} and σ_w; i.e., the simulated slopes for the neutral cases are closer to the observed one (Figs. 6b, d, 7), which is consistent with the observation in Mahrt et al. (2013). However, the vertical decrease of the slopes of the $V_{\text{TKE}}(z)-V(z)$ and $\sigma_w(z)-V(z)$ relationships remains similar between $z_0 = 0.05$ m and $z_0 = 0.5$ m.

To further study the $V_{\text{TKE}}(z)-V(z)$ relationship for the stable case, we compare the simulated $\theta_*(z)$, which is strongly related to temperature fluctuations and TPE as observed in S12, as a function of $V(z)$ in comparison with the observed $\theta_*(z)-V(z)$ relationship in S12

Fig. 6 Regressed relationships **a**, **b** between $V_{\text{TKE}}(z)$ and horizontal wind speed $V(z)$, and **c**, **d** between the standard deviation of the vertical velocity $\sigma_w(z)$ and $V(z)$ at various heights under the stable (*dashed lines*) and the neutral (*solid lines*) conditions in (**a**, **c**), and under the neutral conditions with the roughness length $z_0 = 0.05$ m (*solid lines*) and $z_0 = 0.5$ m (*dashed lines*) in (**b**, **d**). The 5-min mean data from the last hour of each simulation are used. The *vertical lines* present the standard deviations of $V_{\text{TKE}}(z)$ in (**a**, **b**), and of $\sigma_w(z)$ in (**c**, **d**) for each V_g case. The *solid grey line* in each panel represents the relationship at height of 20 m with the threshold horizontal wind speed V_s that delimits the stable [$V(z) < V_s(z)$] and near-neutral [$V(z) > V_s(z)$] regimes observed in S12

(Fig. 8a). The simulated $\theta_*(z)-V(z)$ relationship confirms that the stable case is actually similar to the near-neutral regime in S12, where $\theta_*(z)$ decreases with $V(z)$. As explained in S16, the observed decrease of $\theta_*(z)$ with $V(z)$ is due to reduction of the vertical temperature gradient by large coherent eddies generated by bulk shear $V(z)/z$ when $V(z) > V_s(z)$. Examination of the relationship between $V_{\text{TKE}}(z)$ and the vertical temperature gradient, $\partial\theta(z)/\partial z$, indicates that the increase of $V_{\text{TKE}}(z)$ with $V(z)$ for the stable cases is indeed associated with the decrease of $\partial\theta(z)/\partial z$ (Fig. 8b), even though the temperature in the stable cases is not even nearly uniform in the vertical. As the increase of the simulated $V_{\text{TKE}}(z)$ with $V(z)$ is associated with not only the increased turbulent energy generation with $V(z)$ but also the significant reduction of the vertical temperature gradient and TPE compared with the observed increase of TKE with $V(z)$ only, the simulated $V_{\text{TKE}}(z)$ increases faster with $V(z)$ in the stable cases compared with the neutral ones (Figs. 6a, c, 7).

5.2 Spectral Analysis of Resolved w

To further investigate the slopes of the $V_{\text{TKE}}(z)-V(z)$ and $\sigma_w(z)-V(z)$ relationships with z and to examine the size of the dominant turbulent eddies at each z in comparison with
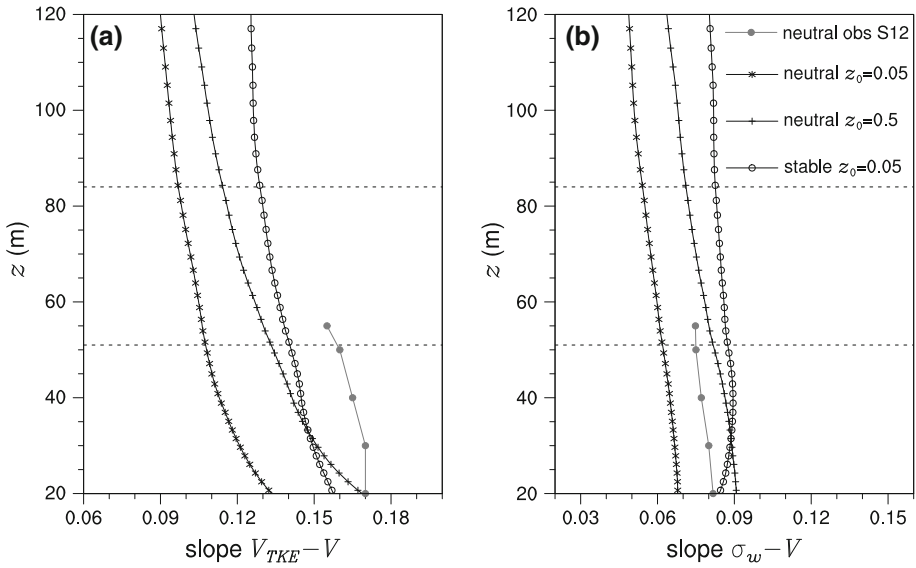
Fig. 7 Regressed slopes of **a** the $V_{\text{TKE}}(z)$–$V(z)$ and **b** $\sigma_w(z)$–$V(z)$ relationships with the roughness length of $z_0 = 0.5$ and $z_0 = 0.05$ m for the neutral cases and $z_0 = 0.05$ m for the stable cases in comparison with the observed ones from the near-neutral regime in S12 (*grey dotted line*)
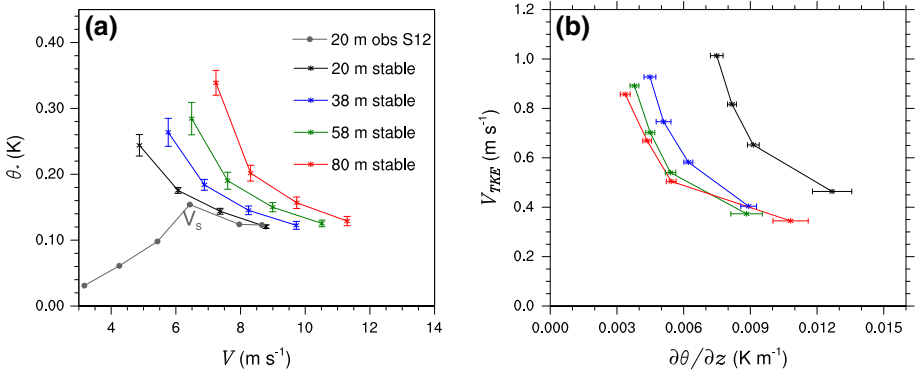

Fig. 8 Regressed relationships **a** between $\theta_*(z)$ and $V(z)$, and **b** between $V_{\text{TKE}}(z)$ and $\partial\theta/\partial z(z)$ at different heights in the stable simulations. The *vertical lines* represent the standard deviations of $\theta_*(z)$ for each V_g in **a**. The *horizontal lines* represent the standard deviations of $\partial\theta/\partial z(z)$ for each V_g in (**b**). The *dotted grey line* in **a** represents the observed relationship at height of 20 m with the threshold horizontal wind speed V_s in S12

the observation in S12, we examine the spectral peak of the resolved w as a function of the normalized wavenumber kz for A-neutral and A-stable simulations at the heights shown in Fig. 9. The spatial spectra are calculated using the resolved w along the wind direction across the middle of the domain from the output at every 1 min averaged over the 9th hour of each simulation. Using the output at every second does not make any important difference.

S12 found that the spectral peak of w in the near-neutral atmosphere under strong winds occurs at a constant value of fz/V, which is kz if the Taylor hypothesis is applied. The observed z independence of the spectral peak frequency or wavenumber implies that the length scale of the dominant turbulent eddies scales with z. S16 further confirmed the contribution
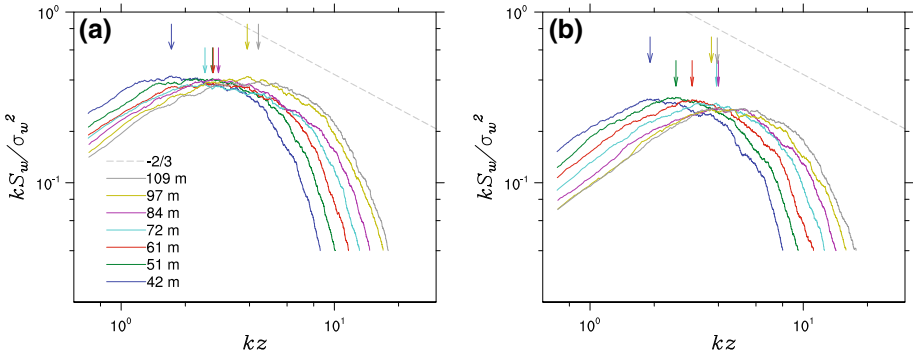
Fig. 9 Normalized power spectra of the resolved vertical velocity kS_w/σ_w^2 as a function of normalized wavenumber kz at various heights z for **a** the A-neutral simulation and **b** the A-stable simulation. The *dashed grey line* indicates the theoretical isotropic spectrum of $-2/3$. *Arrows* in *different colours* indicate spectral peaks at the heights of the corresponding colours
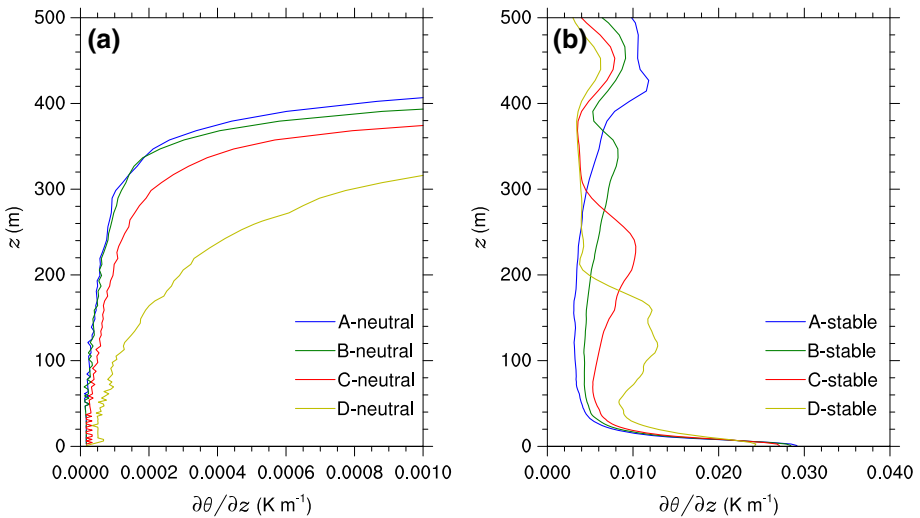
Fig. 10 Vertical temperature gradient profiles for **a** the neutral and **b** the stable cases in response to the four geostrophic winds (A, B, C, and D)

of relatively large coherent eddies to turbulent mixing by studying vertical coherences of vertical and horizontal wind components, and temperature. S12 and S16 also found that the w spectral peak in the SBL shifts to higher frequency compared with the neutral spectrum at the same z, as the size of turbulent eddies decreases with increasing stratification.

Because the contribution of the subgrid σ_w^2 to the total σ_w^2 is about 10 % in the layer between $z \approx 40$ m and h for A-neutral and A-stable simulations (Fig. 5d), the lack of the fine spatial contribution to the calculated spatial spectra of the resolved w at high wavenumbers is evident in the relatively fast decrease of the spectra with kz at the high-wavenumber end (the $-2/3$ decease is marked by the grey lines in Fig. 9). Since we are interested only in w spectral peaks, which are at relatively low wavenumbers, especially for A-neutral simulation, the spatial spectral peaks of resolved w above $z \approx 40$ m are not significantly influenced by the performance of the subgrid scheme, and the spectral correction proposed by Chow et al.

(2005) is not performed here. Because the size of turbulence eddies is increasingly smaller with increasing stratification and increasing z (S12 and S16), the impact of small turbulent eddies on the resolved w spectra would become increasingly important with z under stable conditions. Thus, we do not examine the resolved w spectra for A-stable above 84 m.

We find that the values of kz for the simulated w spectral peaks are close together in the layer between 51 and 84 m for A-neutral simulation (Fig. 9a), and shift towards high wavenumber for A-stable simulation compared with the A-neutral simulation at the same height, as observed in S12 (Fig. 9b). However, above 84 m, the values of the resolved w spectral peaks from A-neutral simulation shift toward higher wavenumber. By examining the vertical variation of $\partial\theta/\partial z$ with z for A-neutral simulation, we find that $\partial\theta/\partial z$ is small below about 80 m, and increases with z systematically, especially above 400 m, where the 200-m damping layer is applied (Fig. 10a). The contribution of increasingly large turbulent eddies to turbulent mixing toward nearly neutral is also evident in the relatively large values of the resolved w spectra at the lowest kz from A-neutral simulation compared with those from A-stable simulation. Because the contribution of small eddies to turbulent intensity increases with decreasing height, as observed by Sun et al. (2013), the apparent shift of the resolved w spectral peak at 42 m toward lower kz could be due to the lack of contributions from eddies smaller than 6–$7\Delta x$ in the resolved w spectrum.

6 Discussion

6.1 Development of the SBL

Although the simulated SBL captures the expected weak turbulence, downward heat flux, and vertical increase of the potential temperature, examination of the simulated relationships between $V_{TKE}(z)$ and $V(z)$ (Fig. 6a) and between $\theta_*(z)$ and $V(z)$ (Fig. 8a) suggests that their responses to the wind-speed increase actually resemble the observed nearly neutral atmosphere, not the observed stable atmosphere. The increase of the downward sensible heat flux with increasing wind (Fig. 4b) maintains the positive vertical temperature gradient such that the SBL does not undergo transition to a nearly neutral state as observed in S16 (Sect. 1). Comparing with the observation in S16, this dilemma is due to the unrealistic formation of the stable stratification from the unrealistic thermal coupling at the surface through turbulent heat transfer instead of molecular thermal conduction. As described by Geiger et al. (1995) [its first edition is Geiger (1927)] and Sun et al. (1995), molecular thermal conduction is responsible for the heat exchange at the surface; i.e., the generation of cold air from the cooling surface is due to molecular thermal conduction. Turbulent mixing is much more efficient in transferring heat than molecular thermal conduction, but is not effective at the surface.

According to observations, as explained in S16, when $V(z)$ is low, the shear-generated turbulent mixing transfers the cold air accumulated near the surface from molecular thermal conduction upward. The turbulent heat transfer vertically redistributes the cold air from a thin to a thicker layer, and leads to the development of the SBL until turbulent mixing is so strong that the cold air is spread vertically quickly, resulting in a well-mixed layer with a nearly vertically invariant temperature. In other words, molecular thermal conduction is responsible for generating cold air over a cooling surface and turbulent heat transfer is responsible for forming the SBL; i.e., the observed vertical temperature gradient is determined by fast turbulent mixing. Turbulent heat transfer, not molecular thermal conduction, can be

approximately parametrized by the Monin-Obukhov bulk relation with vertical aerodynamic temperature differences. In the simulations, using the temperature difference between the surface radiation temperature and the air temperature at the lowest grid point, as is commonly done in numerical parametrization, is equivalent to equating the slow molecular thermal conduction process with the efficient turbulent heat transfer process. This unrealistic thermal coupling at the surface maintains the stable stratification near the surface as if there were always cold air at the surface as long as there are non-zero wind speed and an air–surface temperature difference regardless of whether molecular thermal conduction can generate cold air fast enough for turbulent heat transfer. In our SBL simulations, in contrast, the stronger the wind speed is, the higher the cold air is transported upward, and the vertical temperature gradient can always be maintained even with high wind speeds. In reality, steady strong mixing would lead to the rapid vertical transport of cold air upward and warm air downward, whereas the heat exchange at the cooling surface through slow molecular thermal conduction cannot supply cold air fast enough to maintain the strong stable stratification. As a result, the simulation fails to capture the transition of the SBL to the observed near-neutral atmosphere with high wind speed, i.e., the HOST pattern in S12 and S16.

The failure to capture the observed stable atmosphere is also partly because of the lack of a small V_g in the simulation constrained by the runaway cooling issue (Derbyshire 1990), which is also possibly related to the unrealistic thermal coupling at the surface in generating excessive cooling near the surface for weak turbulent mixing associated with weak winds. This result highlights the different roles of molecular thermal conduction and turbulent heat transfer in establishing the observed SBL. Thus, careful parametrization of the development of the SBL that resembles the nighttime atmosphere needs to be reconsidered.

Estimating observed turbulent heat fluxes by the Monin-Obukhov bulk relation with a surface radiation temperature instead of an aerodynamic temperature requires a "tuned" thermal roughness, which varies significantly with the surface radiation temperature (Sun and Mahrt 1995). The thermal roughness associated with the surface radiation temperature varies by several orders of magnitude daily because the surface radiation temperature varies diurnally and is a function of surface vegetation cover, soil properties, and solar angle. Therefore, it is not practical to force the Monin-Obukhov bulk relation that is intended to describe turbulent mixing to describe molecular thermal conduction by varying the thermal roughness constantly.

6.2 Damping Layer

Through the above investigations of the WRF–LES–EVTS simulations, impacts of the damping layer are evident in (i) the increase of the downward heat flux with z (Fig. 4b), (ii) the sharp increase of the ratios of the subgrid to total $\sigma_v^2(z)$ and $\sigma_w^2(z)$ around the bottom of the damping layer (Fig. 5b, d), (iii) the shift of the w spectral peaks toward higher wavenumber as z increases (Fig. 9a), and (iv) the sharp increase of the vertical temperature gradient around the bottom of the damping layer (Fig. 10a) for the neutral simulations, especially for A-neutral when turbulence is strongest and is dominated by relatively large coherent eddies. This evidence suggests that the damping layer reduces the turbulence intensity of large coherent eddies by absorbing vertical turbulent motions, which is equivalent to reducing TKE through increasing TPE in a stably stratified flow. As a result of the heat transfer associated with its initial temperature profile, the air layer toward the damping layer is less well mixed from its increasing stable atmosphere compared with the layer below. Because of the resulting increasing stable stratification with z as a result of the damping effect (Fig. 10a), the size of turbulent eddies decreases, leading to the shift of the w spectra towards higher

wavenumber, and the vertical increase of the subgrid contribution to the total turbulent variables. Consequently, the slope of the $V_{TKE}(z)-V(z)$ relationship decreases with z in response to the increase in TPE as a result of the damping layer for all the neutral simulations (Fig. 7a). The relatively small increase of $V_{TKE}(z)$ versus $V(z)$ with z for the simulated neutral cases compared with the observed value in S12 (Fig. 7a) could also be related to the difference between the constant and the vertically varying pressure gradients in the simulations and in the atmosphere, respectively, i.e., effects of atmospheric baroclinicity on the vertical variation of wind shear, as discussed in Sun et al. (2013).

As turbulence is generated by wind shear at the surface, and the size of turbulence eddies is smaller in the stable atmosphere, the initial temperature profile far away from the surface should remain unchanged from its initial value, especially under very stable conditions. The weak turbulent mixing near the surface and the constant cooling of the surface only influence the stable atmosphere near the surface. The simulations indeed demonstrate that, for D-stable when the wind speed is lowest, the increase of the final temperature profile with z at the bottom of the initial temperature inversion layer around $z = 175$ m is similar to its initial value (Fig. 3b), and the vertical temperature gradient there approximately equals its initial value of 0.01 K m^{-1} (Fig. 10b); i.e., the effect of the damping layer at the top 200 m is not as dramatic for the stable simulations near the surface as for the neutral ones. As the downward turbulence intensity above 400 m is suppressed through the damping mechanism, the downward heat transfer of warm air associated with the initial temperature profile is suppressed, but not the upward transport of the cold air. Therefore, there is a cooling effect at the top of the domain, and the temperature above $z \approx 250$ m decreases below its initial value even for D-stable simulation (Fig. 3b). As wind speed increases, the cooling effect of the damping layer on turbulent mixing could be mixed with the upward turbulent transport of the cold air generated at the surface. Thus, it is ambiguous to investigate physical processes in determination of the turbulent intensity there.

The WRF–LES–EVTS simulations demonstrate that, because turbulent eddies are relatively large under nearly neutral and unstable conditions, the undesirable impact of the damping layer on boundary-layer mixing needs to be considered carefully. By absorbing undesirable numerical waves, the turbulence energy conservation can be affected through large coherent eddies even near the surface.

7 Summary and Conclusions

The WRF–LES modelling system has been used to study the vertical structure of turbulence in the neutral and the stable ABL. We validate the results against the LES models for the reference weakly stable case of GABLS in Beare et al. (2006). Beyond the existing LES studies in literature that reproduce neutral and stable boundary layers, we investigate the simulated turbulence intensity with increasing wind speed through a range of geostrophic forcing in the neutral and stable atmosphere and compare the results with the observations from CASES-99 (Sun et al. 2012, 2016). We focus on resolved eddies to avoid any uncertainty of the subgrid scheme. The WRF–LES model is able to reproduce the neutral and moderately stable atmosphere in terms of the vertical variations of horizontal wind speed, temperature, and fluxes of momentum and heat.

The relationship between $V_{TKE}(z)$ and $V(z)$ in the neutral simulations suggests that the simulated neutral atmosphere is approximately consistent with the observed one near the surface in S12 and S16. The near-constant value of kz for the resolved w spectral peaks also

supports the idea of the important role of bulk shear, $V(z)/z$, in turbulence generation in the nearly neutral atmosphere.

The damping layer that is commonly used to absorb undesirable downward-propagating numerical waves at the top of the simulation domain can impact turbulent momentum flux as well as downward turbulent heat transfer associated with the initial temperature profile and the simulated heat transfer below the damping layer. The influence of the damping layer on the simulated turbulent mixing in the ABL is significant when turbulent eddies are large, such as under neutral condition, and is relatively small near the surface under the most stable simulation as the dominant turbulent eddies are relatively small.

Even though the simulated SBL with the specified surface cooling rate captures the main characteristics of the observed SBL, the simulated stable boundary layer does not capture the observed heat transfer with increasing wind speed due to the unrealistic formulation of low molecular thermal contribution in forming the cold air near the surface by applying the fast turbulent heat transfer parameterized through the Monin-Obukhov bulk relation. As a result, the simulated SBL cannot reproduce the observed weak increase of $V_{TKE}(z)$ with $V(z)$ and the decrease of $\theta_*(z)$ with $V(z)$ in the SBL, and the transition to the near-neutral atmosphere with increasing wind speed as observed.

In summary, this study suggests the importance of detailed investigation of physical processes in simulating atmospheric turbulent mixing, the need for an adequate representation of the heat transfer at the surface to achieve the observed SBL and of the SGS turbulence as well, and the necessity for careful design of numerical methods so as to not interfere with physical processes in the considered domain.

References

Andren A (1995) The structure of stably stratified atmospheric boundary layers: a large-eddy simulation study. Q J R Meteorol Soc 121(525):961–985

Basu S, Port-Agel F (2006) Large-eddy simulation of stably stratified atmospheric boundary layer turbulence: a scale-dependent dynamic modeling approach. J Atmos Sci 63:2074–2091

Beare RJ, Macvean MK, Holtslag AA, Cuxart J, Esau I, Golaz JC, Jimenez MA, Khairoutdinov M, Kosovic B, Lewellen D et al (2006) An intercomparison of large-eddy simulations of the stable boundary layer. Boundary-Layer Meteorol 118(2):247–272

Brown A, Derbyshire S, Mason P (1994) Large-eddy simulation of stable atmospheric boundary layers with a revised stochastic subgrid model. Q J R Meteorol Soc 120(520):1485–1512

Chow FK, Street RL, Xue M, Ferziger JH (2005) Explicit filtering and reconstruction turbulence modeling for large-eddy simulation of neutral boundary layer flow. J Atmos Sci 62(7):2058–2077

Cuxart J, Bougeault P, Redelsperger JL (2000) A turbulence scheme allowing for mesoscale and large-eddy simulations. Q J R Meteorol Soc 126(562):1–30

Derbyshire SH (1990) Nieuwstadt's stable boundary layer revisited. Q J R Meteorol Soc 116(491):127–158

Garratt JR (1992) The atmospheric boundary layer, Cambridge atmospheric and space science series. Cambridge University Press, UK, 316 pp

Geiger R (1927) The climate near the ground, 1st edn. Vieweg, Braunschweig

Geiger R, Aron RH, Todhunter P (1995) The climate near the ground, 5th edn. Harvard University Press, Cambridge, 528 pp

Huang J, Bou-Zeid E (2013) Turbulence and vertical fluxes in the stable atmospheric boundary layer. Part I: a large-eddy simulation study. J Atmos Sci 70(6):1513–1527

Jimenez MA, Cuxart J (2005) Large-eddy simulations of the stable boundary layer using the standard Kolmogorov theory: range of applicability. Boundary-Layer Meteorol 115(2):241–261

Kirkil G, Mirocha J, Bou-Zeid E, Chow FK, Kosovic B (2012) Implementation and evaluation of dynamic subfilter-scale stress models for large-eddy simulation using WRF. Mon Weather Rev 140(1):266–284

Kosović B (1997) Subgrid-scale modelling for the large-eddy simulation of high-reynolds-number boundary layers. J Fluid Mech 336(1):151–182

Kosović B, Curry JA (2000) A large eddy simulation study of a quasi-steady, stably stratified atmospheric boundary layer. J Atmos Sci 57(8):1052–1068

Lilly DK (1967) The representation of small scale turbulence in numerical simulation experiments. In: Proceedings of the IBM scientific computing symposium on environmental sciences 320-1951, 195-210

Liu Y, Warner T, Liu Y, Vincent C, Wu W, Mahoney B, Swerdlin S, Parks K, Boehnert J (2011) Simultaneous nested modeling from the synoptic scale to the LES scale for wind energy applications. J Wind Eng Ind Aerodyn 99(4):308–319

Mahrt L (1998) Nocturnal boundary-layer regimes. Boundary-Layer Meteorol 88(2):255–278

Mahrt L, Thomas C, Richardson S, Seaman N, Stauffer D, Zeeman M (2013) Non-stationary generation of weak turbulence for very stable and weak-wind conditions. Boundary-Layer Meteorol 147(2):179–199

Mason P, Derbyshire S (1990) Large-eddy simulation of the stably-stratified atmospheric boundary layer. Boundary-Layer Meteorol 53(1–2):117–162

Mirocha JD, Kosović B (2010) A large-eddy simulation study of the influence of subsidence on the stably stratified atmospheric boundary layer. Boundary-Layer Meteorol 134(1):1–21

Mirocha JD, Lundquist J, Kosovic B (2010) Implementation of a nonlinear subfilter turbulence stress model for large-eddy simulation in the advanced research WRF model. Mon Weather Rev 138(11):4212–4228

Mirocha JD, Kirkil G, Bou-Zeid E, Katopodes Chow F, Kosovic B (2013) Transition and equilibration of neutral atmospheric boundary layer flow in one-way nested large-eddy simulations using the Weather Research and Forecasting model. Mon Weather Rev 141:918

Mirocha JD, Kosović B, Kirkil G (2014) Resolved turbulence characteristics in large-eddy simulations nested within mesoscale simulations using the weather research and forecasting model. Mon Weather Rev 142(2):806–831

Moeng C, Dudhia J, Klemp J, Sullivan P (2007) Examining two-way grid nesting for large eddy simulation of the PBL using the WRF model. Mon Weather Rev 135(6):2295–2311

Muñoz-Esparza D, Kosović B, García-Sánchez C, van Beeck J (2014) Nesting turbulence in an offshore convective boundary layer using large-eddy simulations. Boundary-Layer Meteorol 151(3):453–478

Nieuwstadt FTM (1985) A model for the stationary, stable boundary layer. In: Hunt JCR (ed) Turbulence and diffusion in stable environments. Oxford University Press, Oxford, pp 149–173

Ostrovsky L, Troitskaya YI (1987) A model of turbulent transfer and dynamics of turbulence in a stratified shear-flow. Izvestiya Akademii Nauk Sssr Fizika Atmosfery I Okeana 23(10):1031–1040

Poulos GS, Blumen W, Fritts DC, Lundquist JK, Sun J, Burns SP, Nappo C, Banta R, Newsom R, Cuxart J et al (2002) CASES-99: a comprehensive investigation of the stable nocturnal boundary layer. Bull Am Meteorol Soc 83(4):555–581

Saiki EM, Moeng CH, Sullivan PP (2000) Large-eddy simulation of the stably stratified planetary boundary layer. Boundary-Layer Meteorol 95(1):1–30

Skamarock W, Klemp J, Dudhia J, Gill D, Barker D, Duda M, Huang X, Wang W, Powers J (2008) A description of the Advanced Research WRF Version 3, NCAR technical note. Mesoscale and Microscale Meteorology Division, National Center for Atmospheric Research, Boulder

Skamarock WC (2004) Evaluating mesoscale NWP models using kinetic energy spectra. Mon Weather Rev 132(12):3019–3032

Smagorinsky J (1963) General circulation experiments with the primitive equations. Mon Weather Rev 91(3):99–164

Stull RB (1988) An introduction to boundary layer meteorology. Kluwer Academic Publishers, Dordrecht

Sun J (2011) Vertical variations of mixing lengths under neutral and stable conditions during CASES-99. J Appl Meteorol Clim 50(10):2030–2041

Sun J, Mahrt L (1995) Determination of surface fluxes from the surface radiative temperature. J Atmos Sci 52:1096–1106

Sun J, Esbensen SK, Mahrt L (1995) Estimation of surface heat flux. J Atmos Sci 52:3162–3171

Sun J, Mahrt L, Banta RM, Pichugina YL (2012) Turbulence regimes and turbulence intermittency in the stable boundary layer during CASES-99. J Atmos Sci 69(1):338–351

Sun J, Lenschow DH, Mahrt L, Nappo C (2013) The relationships among wind, horizontal pressure gradient, and turbulent momentum transport during CASES-99. J Atmos Sci 70(11):3397–3414

Sun J, Mahrt L, Nappo C, Lenschow DH (2015) Wind and temperature oscillations generated by wave-turbulence interactions in the stably stratified boundary layer. J Atmos Sci 72(2014):1484–1503

Sun J, Lenschow DH, LeMone MA, Mahrt L (2016) The role of large-coherent-eddy transport in the atmospheric surface layer based on cases-99 observations. Boundary-Layer Meteorol. doi:10.1007/s10546-016-0134-0

Talbot C, Bou-Zeid E, Smith J (2012) Nested mesoscale large-eddy simulations with WRF: performance in real test cases. J Hydrometeorol 13(5):1421–1441

Van de Wiel B, Moene A, Hartogensis O, De Bruin H, Holtslag A (2003) Intermittent turbulence in the stable boundary layer over land. Part III: a classification for observations during CASES-99. J Atmos Sci 60(20):2509–2522

Yagüe C, Viana S, Maqueda G, Lazcano MF, Morales G, Rees JM (2007) A study on the nocturnal atmospheric boundary layer: SABLES2006. Física de la Tierra 19:37–53

Zilitinkevich S, Elperin T, Kleeorin N, Rogachevskii I (2007) Energy-and flux-budget (EFB) turbulence closure model for stably stratified flows. Part I: steady-state, homogeneous regimes. Boundary-Layer Meteorol 125(2):167–191